

# XMM–Newton timing mode observations of Mrk 421

W. Brinkmann<sup>1</sup>, I. E. Papadakis<sup>2,3</sup>, C. Raeth<sup>1</sup>, P. Mimica<sup>4</sup>, and F. Haberl<sup>1</sup>

<sup>1</sup> Max–Planck–Institut für extraterrestrische Physik, Postfach 1312, 85741 Garching, FRG, Germany  
e-mail: wpb@mpe.mpg.de

<sup>2</sup> IESL, FORTH, 711 10 Heraklion, Crete, Greece

<sup>3</sup> Physics Department, University of Crete, 710 03 Heraklion, Crete, Greece

<sup>4</sup> Max–Planck–Institut für Astrophysik, Postfach 1317, 85741 Garching, FRG, Germany

Received 25 January 2005 / Accepted 14 July 2005

## ABSTRACT

We present the results of a detailed temporal analysis of the bright BL Lac object Mrk 421 using the three available long timing mode observations by the EPIC PN camera. This detector mode is characterized by its long life time and is largely free of photon pile-up problems. The source was found in different intensity and variability states differing by up to more than a factor of three in count rate. A time resolved cross correlation analysis between the soft and hard energy bands revealed that the characteristics of the correlated emission, with lags of both signs, change on time scales of a few  $10^3$  s. Individual spectra, resolved on time scales of  $\sim 100$  s, can be quite well fitted by a broken power law and we find significant spectral variations on time scales as short as  $\sim 500$ – $1000$  s. Both the hard and the soft band spectral indices show a non-linear correlation with the source flux. A simple power law model of the form  $\Gamma \propto \text{flux}^{-a}$  with  $a_{\text{hard}} \sim 0.13$  and  $a_{\text{soft}} \sim 0.22$  describes rather well the observed trend of decreasing  $\Gamma$  values with increasing flux, which appear to “saturate” at the same limiting value of  $\Gamma \sim 1.8$  at the highest flux levels. A comparison of the observed light curves with numerical results from relativistic hydrodynamic computer simulations of the currently favored shock-in-jet models indicates that any determination of the jet’s physical parameters from “simple” emission models must be regarded with caution: at any time we are seeing the emission from several emission regions distinct in space and time, which are connected by the complex hydrodynamic evolution of the non-uniform jet.

**Key words.** BL Lacertae objects: individual: Mrk 421 – X-rays: galaxies – radiation mechanisms: non-thermal

## 1. Introduction

BL Lacs are radio-loud AGN dominated by relativistic jets seen at small angles to the line of sight (Urry & Padovani 1995). They are characterized by large luminosities, large and variable polarization, and strong variability. A substantial part of the information we possess about these objects is obtained from the analysis of temporal variations of the emission and the combined spectral and temporal information can greatly constrain the jet physics. Time scales are related to the crossing time of the emission regions which depend on wavelength and/or the time scales of the relevant physical processes. The measured lags between the light curves at different energies as well as spectral changes during intensity variations allow us to probe the physics of particle acceleration and radiation in the jet.

Mrk 421 is the brightest BL Lac object at X-ray and UV wavelengths and it is the first extragalactic source discovered at TeV energies (Punch et al. 1992). The nearby ( $z = 0.031$ ) object was observed by almost all previous X-ray missions and shows remarkable X-ray variability correlated with strong activity at TeV energies (e.g., Takahashi et al. 1996; Maraschi et al. 1999). Structure function and power density spectrum analyses indicate a roll-over with a time scale of the order of

1 day or longer (Cagnoni et al. 2001; Kataoka et al. 2001) which seems to be the time scale of the successive flare events. On shorter time scales less power in the variability is found with a steep slope of the power density spectrum  $\sim f^{-(2-3)}$  (Tanihata 2002; Brinkmann et al. 2003).

The smooth featureless continuum spectra of Mrk 421 from the radio to the X-ray band imply that the emission in these energy bands is due to relativistic particles radiating via the Synchrotron process; the hard X-rays and  $\gamma$ -rays are likely to be produced by inverse Compton scattering of synchrotron photons by the same electrons (Ulrich et al. 1997 and references therein). Broken power law models provided better fits to the ASCA 0.6–7 keV data than a simple power law (Takahashi et al. 1996) with a break energy of  $\sim 1.5$  keV, and the change of the power law index at the break point is  $\Delta\Gamma \sim 0.5$ , i.e., the spectrum is steeper at higher energies.

With the wider energy range of BeppoSAX it became clear that the simple models are not adequate descriptions of the downward curved Synchrotron spectra (Fossati et al. 200b) and continuously curved shapes had to be employed (Inoue & Takahara 1996; Tavecchio et al. 1998). The synchrotron peak energy varied between 0.4–1 keV, the spectral index at an

energy of 5 keV between  $2.5 \leq \Gamma \leq 3.2$ . Both quantities are correlated with the X-ray flux: with increasing flux the synchrotron peak shifts to higher energies and the spectrum gets flatter at higher energies.

The emission of the soft X-rays is generally well correlated with that of the hard X-rays and lags it by 3–4 ks (Takahashi et al. 1996, 2000; Zhang et al. 1999; Malizia et al. 2000; Kataoka et al. 2000; Fossati et al. 2000a; Cui 2004), however, significant lags of both signs were detected from several flares (Tanihata et al. 2001; Takahashi et al. 2000).

These results were obtained from data with relatively low signal-to-noise ratio, integrated over wide time intervals (typically one satellite orbit) and by analyzing data from prominent flares with time scales of a day. Recently, *XMM–Newton* with its high sensitivity, spectral resolving power and broad energy band provided uninterrupted data with high temporal and spectral resolution. In an analysis of the early *XMM–Newton* data (Brinkmann et al. 2001) for the first time the evolution of intensity variations could be resolved on time scales of  $\sim 100$  s. Temporal variations by a factor of three at highest X-ray energies were accompanied by complex spectral variations with only a small time lag of  $\tau = 265^{+116}_{-102}$  s between the hard and soft photons. Sembay et al. (2002) confirmed these short lags in an analysis of a larger set of *XMM–Newton* observations of Mrk 421 and they show that the source exhibits a rather complex and irregular variability pattern – both temporarily and spectrally. From *XMM–Newton* observations of PKS 2155-304 (Edelson et al. 2001) suggest that previous claims of soft lags with time scales of  $\sim$  hours might be an artifact of the periodic interruptions of the low-Earth orbits of the satellites every  $\sim 1.6$  h. This claim was questioned by (Zhang et al. 2004) who show that, although periodic gaps introduce larger uncertainties than present in evenly sampled data, lags on time scales of hours cannot be the result of periodic gaps.

In an extended analysis of all available *XMM–Newton* PN observations of Mrk 421 (Brinkmann et al. 2003) split up the individual light curves into shorter sub-intervals in which the flux appeared to show some similar specific behavior. The cross-correlation analysis of these individual soft and hard band light curves demonstrated that they are in general well correlated at zero lags, but sometimes the hard band variations lead the soft band variations by typically  $\sim 5$  min, in two cases the soft band lead the hard band variations. The delays appear to be correlated with a harder spectrum during higher intensities. Recently, Ravasio et al. (2004) used three *XMM–Newton* observations in Nov./Dec. 2002 when Mrk 421 was highly variable. During two large flares the source showed strong spectral evolution and temporal lags between the different energy band variations of both signs, with lags of up to more than 1000 s.

In this paper we will present a detailed analysis of the three currently available XMM data sets on Mrk 421 in which the PN camera was operated in timing mode. We re-processed the data and used the most recent response functions. In previous observations of Mrk 421 even the high time resolution of the PN in small window mode sometimes proved to be insufficient to prevent photon pile up when the source was in a high intensity state. This led to a reduction of the signal to noise ratio

for the spectral data and to frequent unpredictable large observational gaps in the light curves, due to the extremely high work load of the on-board electronics (FIFO overflows) and the limits of the telemetry rate (counting mode). Timing mode data have a very high photon collecting efficiency of 99.5% of the frame time and do not suffer from pile-up problems which would, with other detector modes, lead to a substantial loss of data for the extremely high count rates of Mrk 421.

Two of the data sets, that of orbit 84 as well as the short flare in orbit 546 have been presented previously (Brinkmann et al. 2003 and Ravasio et al. 2004, respectively), however, only in a more limited analysis and without special emphasis on their short time scale behavior. The third dataset, from orbit 807, when the source is extremely bright, has not been published before. In our analysis we take full advantage of the excellent statistical quality of the timing mode data sets and, in particular, we will for the first time analyse the data on time intervals considerably shorter than the individual observations as the source exhibits changes in its spectral properties on time scales down to a few thousand seconds. We will study the spectral slope variability on time scales as short as  $\lesssim 1000$  s and how that correlates with the flux variations; we search the cross correlation function over very short periods and discuss how it changes with time as the flux varies.

We will first present the data and demonstrate the spectral complexity of Mrk 421 in broad band spectral fits. We will discuss the “standard” cross-correlation analysis of the data which is commonly used to investigate the cross-links between the hard and soft band light curves and will then introduce a sliding-window technique to study the cross-correlations on shorter time scales. In Sect. 4 we will present a detailed analysis of the source properties using temporally resolved spectral analyses. We then discuss these results in the framework of the shock-in-jet model with some emphasis on numerical simulations of the hydrodynamic evolution of non-uniform relativistic jets. Final conclusions will be given in Sect. 6.

## 2. The XMM–Newton observations

Mrk 421 was observed repeatedly during the XMM–Newton mission, mostly as a calibration source for the RGS. During three of these observations the PN camera was operated in timing mode, once with a thick filter (orbit 84), the other times with medium filter. This mode has the advantage that even at highest source count rates, pile up, and thus spectral distortions, can be neglected. The details of the observations are given in Table 1, where we first list the orbit in which the observation took place, the date of the observation, the instrument settings and the duration of the observation. Due to the high count rate from Mrk 421 the detector falls frequently into counting mode, which introduces gaps of typically 21 s duration into the data stream. This happens when the read-out buffer is 75% full, and the rate at which this occurs depends critically on the work load of the detector. For example, in orbit 807, with the extremely high count rate on the chip, about every 20 s of data are followed by this  $\sim 21$  s gap; the observation consists of  $\sim 1800$  of these “elementary observation intervals” (EOIs). In orbit 546, with its much lower count rate, each EOI consists of  $\sim 100$  s

**Table 1.** Details of the observations.

Orbit	Observing date (UT)	PN mode	Filter	Duration [ ks ]	Live time [ ks ]	count rate on chip	source count rate [0.6–10 keV]*
084	May 25, 2000: 03:53–10:11	Timing	Thick	22.4	16.78	373.3	221.6±0.1
546	Dec. 1, 2002: 23:18–18:44 <sup>†</sup>	Timing	Medium	71.2	59.00	303.9	176.9±1.3
807	May 6, 2004: 02:38–21:11	Timing	Medium	66.7	25.63	841.3	491.7±0.2

<sup>†</sup> Next day.

\* Background subtracted source count rate for the spectral fit.

data, followed by the gap. Correspondingly, the Live Time of the detector (Col. 6) is rather short for orbit 807 and highest for orbit 546. Column 7 gives the average count rate recorded on the chip when no spatial nor quality selection for the photons were made, while in Col. 8 we list the screened, background subtracted source count rates for the total spectral fit in the 0.6–10 keV band.

All data have been reprocessed using XMMSAS version 6.1. For the spectral fits the latest response matrices were used, for which adjustments of the effective areas around the Au edges were made as well as corrections for the thick filter near the Al edge. We selected photons with  $\text{Pattern} \leq 4$  (i.e. singles and doubles) and quality flag = 0. For the source data we selected the photons from rows  $29 \leq \text{RAWX} \leq 45$  for our analysis, as background we used the photons from rows  $2 \leq \text{RAWX} \leq 18$  (for a description of the instrument and the detector modes see (Ehle et al. 2001)). The energy range for all analyses was taken to be  $600 \text{ eV} \leq E \leq 10 \text{ keV}$  as below 600 eV the single-double ratio is not constant and thus gives unreliable results in the spectral analyses. The background count rates in the whole energy band are generally less than  $\sim 1.5\%$  of the source count rates, and even at energies  $\sim 10 \text{ keV}$  they amount to  $\lesssim 10\%$  of the source rates. A few short background flares and the data at the end ( $\geq 60 \text{ ks}$ ) of the observation of orbit 807 were discarded from the spectral analysis presented in Sect. 4.

## 2.1. Orbit integrated properties

To demonstrate the magnitudes of the source variability we present in Fig. 1 the 0.6–10 keV 100 s bin light curves for the three observations with the above photon selection criteria. The counting errors are smaller than the symbol sizes. For comparison with previously published light curves please note that the count rates are dominated by photons at low energies. For example, extending the energy range down to 500 eV would increase the count rate by about 15%, going down to 200 eV nearly doubles the number of counts. The orbit 84 observation was performed with the thick filter; correcting these data to the medium thick filter would result in a factor of typically  $\geq 1.2$  higher count rates.

The light curves are characterized by long term trends lasting for time scales comparable to or longer than the length of the observations and, superimposed on this, of frequent flare like events of relatively regular shape with characteristic time scales of the order of a few thousand seconds. Interestingly,

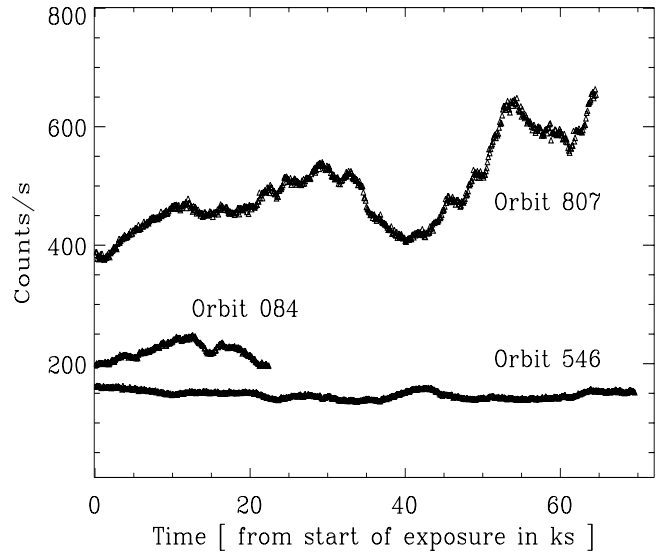


**Fig. 1.** Background subtracted, 0.6–10 keV PN light curves of Mrk 421 with time binning of 100 s. Times are counted from the beginning of the actual exposure. The curves are labeled by the orbit of the observation.

larger variations occur when the source is in a higher state: during orbit 546 the maximum to minimum intensity variations are  $\lesssim \pm 15\%$ , in orbit 84 of  $\sim \pm 20\%$  and in orbit 807 even  $\gtrsim \pm 40\%$ .

## 2.2. Spectral analysis

As mentioned above the spectral behavior of Mrk 421 is rather complex and with increasing data quality more sophisticated spectral models had to be used for the fits. To show the integral spectral behavior of the source during the three observations we present in Fig. 2 the fits to the total data of each orbit to a broken power law. The plotted residuals are heavily rebinned. The deviations between model and data are only of a few percent. The numerical results are given in Table 2. The absorption has been fixed to the galactic value; keeping  $N_{\text{H}}$  as a free parameter results in slightly lower values of  $\chi_{\text{red}}^2$  and slightly higher column densities. Interestingly, the slope changes at the break energy are rather small which might indicate that we see the source near the Synchrotron peak of its SED. Fitting a continuously curved model (Fossati et al. 200b) to the data results in fits of very similar  $\chi_{\text{red}}^2$ , however the residuals indicate that at higher energies the curvature of the spectrum is over-estimated.

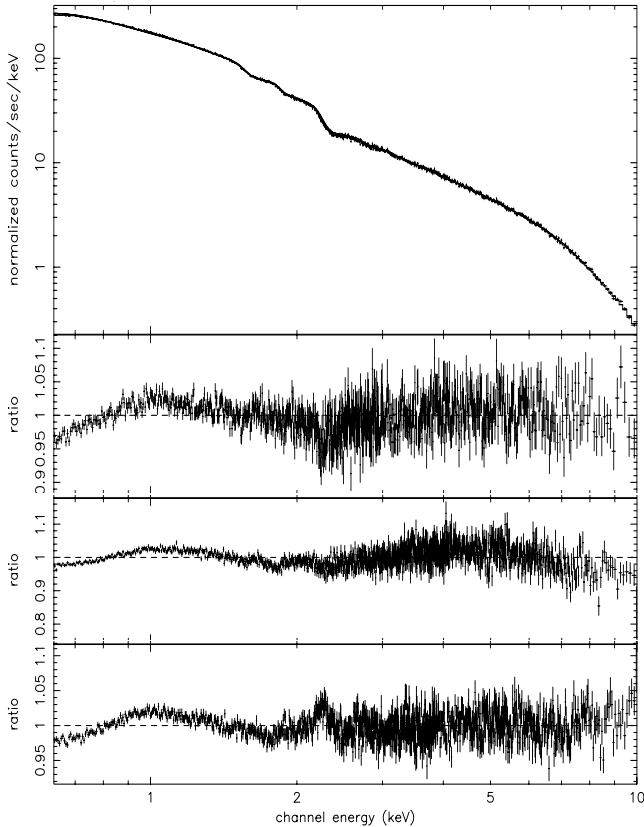


**Fig. 2.** Broken power law model fit to the 0.6–10 keV data during the three observations. The two top figures show the fit and the data to model ratio for orbit 84, the middle panel the ratio for orbit 546, the bottom panel that for orbit 807.

The  $\chi_{\text{red}}^2$  given in Table 2 show that the fits are hardly acceptable which is to a great extent due to the extremely high photon statistics in the soft energy band (for example, there are 13.2 million photons in the orbit 807 spectrum). There is still some uncertainty in the calibration, visible around  $\sim 2$  keV (the Au edge and, possibly, some Si feature at slightly lower energies) and a general convex curved low energy part. Whether this slight extra low energy curvature is in the range of the calibration uncertainties or a “source intrinsic” spectral property cannot be answered yet. The residuals around 2 keV further indicate that these structures are not strictly stationary during the three observations taken over four years. They are likely not source specific but they could be small secular changes of the detector characteristics over these years. (A gain-fit over a limited energy range around 2 keV reduces the residuals strongly). Secondly, the spectral slopes vary with the intensity variations causing some dispersion of the data with respect to the average model. The time resolved fits of a broken power law model to shorter data segments (see Sect. 4) mostly result in  $\chi_{\text{red}}^2 \sim 1.0$ ; thus a broken power law provides an adequate description of these Mrk 421 spectra. The general impression from the above total fits is that the spectrum gets flatter with increasing flux and that the break energy shifts towards higher values.

**Table 2.** Results for the broken power law fits assuming galactic absorption ( $N_{\text{H}} = 1.66 \times 10^{20} \text{ cm}^{-2}$ ).

Orbit	$\Gamma_{\text{soft}}$	$E_{\text{brk}}$ (keV)	$\Gamma_{\text{hard}}$	Norm (1)	$\chi_{\text{red}}^2/\text{d.o.f.}$ (1)
084	$2.257 \pm 0.001$	$4.00 \pm 0.17$	$2.354 \pm 0.009$	0.182	1.22/1584
546	$2.400 \pm 0.009$	$3.37 \pm 0.42$	$2.620 \pm 0.006$	0.108	1.69/1671
807	$1.969 \pm 0.001$	$4.63 \pm 0.19$	$2.027 \pm 0.006$	0.316	1.58/1900

(1): Normalization at 1 keV in ph/keV/cm<sup>2</sup>/s.

### 3. Cross-correlation analysis

In order to investigate the cross-links between the hard and soft band light curves we estimated their Cross-Correlation Function (CCF), using light curves with a 10-s bin size. If a data segment is followed by the typical 21 s long FIFO gap, this is filled with a running mean. We originally chose to work with this small bin size because the signal is rather strong and, secondly, previous cross-correlation analyses between soft and hard band light curves have indicated that, if inter-band delays exist, they are very small (Brinkmann et al. 2003). The following temporal and spectral analyses show, however, that noticeable spectral changes occur on longer time scales of a few hundred seconds. Since the results from the previous section show that the energy spectrum exhibits a significant spectral slope change at energies between 3 and 4 keV (see Table 2), we chose the count rates in the 0.6–2 keV and 4–10 keV bands as representative of the soft and hard band spectral components of the source. This choice of energies further ensures that there is no “spill-over” of flux between the two bands.

We calculated the sample Cross-Correlation Function,  $\text{CCF}(k)$ , as follows:

$$\text{CCF}(k) = \frac{\sum_t (x_{\text{soft}}(t) - \bar{x}_{\text{soft}})(x_{\text{hard}}(t+k) - \bar{x}_{\text{hard}})}{N(k)(\sigma_{\text{soft}}^2 \sigma_{\text{hard}}^2)^{1/2}},$$

$$k = 0, \pm\Delta t, \dots, \pm(N-1)\Delta t.$$

The summation goes from  $t = \Delta t$  to  $(N-k)\Delta t$  for  $k \geq 0$  ( $\Delta t = 10$  s, and  $N$  is the total number of points in the light curve) and the sum is divided by the number of pairs included, i.e.  $N(k)$ . For negative lags  $k < 0$  the summation has to be done over  $x_{\text{soft}}(t+|k|)$  and  $x_{\text{hard}}(t)$ . The variances in the above equation are the source variances, i.e., after correction for the experimental variance. Significant correlation at positive lags means that the soft band variations are leading the hard band.

First, we computed the CCF (up to lags  $\pm 3$  h) using the whole length (i.e. total) soft and hard band light curves. The resulting CCFs are shown in Fig. 3 (the CCF for orbit 84 is similar to Fig. 13 of Brinkmann et al. 2003), while (Ravasio et al. 2004) present in Fig. 9 the CCF of only the “flare” at  $t \sim 42$  ks in orbit 546). Although all three CCFs peak at zero lag, there are clearly definite differences in shape between them. The ranges for the values of the cross-correlation coefficients are different. Further, in orbit 84 the auto-correlation function of the soft band is very similar to the CCF; in the other two

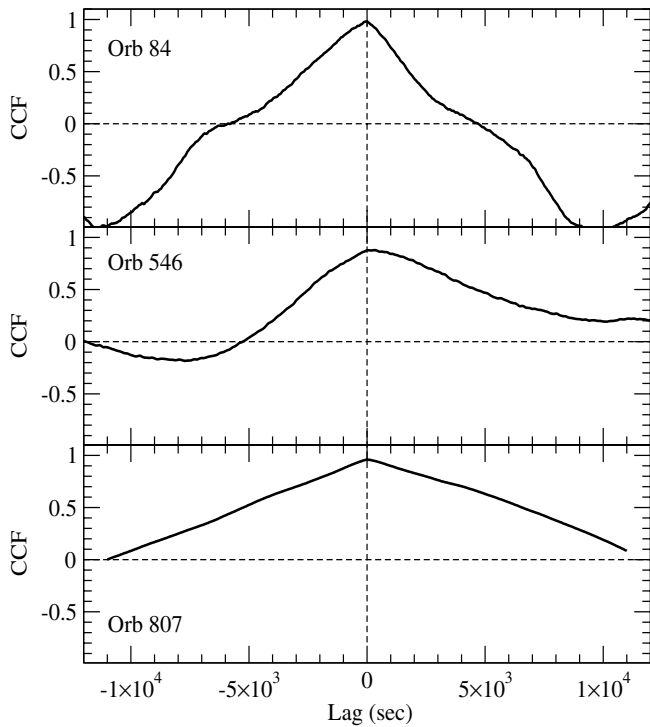


**Fig. 3.** CCF plots for the orbit 84 (top), orbit 546 (middle) and orbit 807 (bottom) observation. The 10 s binned soft and hard band light curves for the total observations were used; the error bars are smaller than the symbol sizes. The curves are labeled by the orbit of the observation.

orbits the CCF is skewed with respect to the ACF in the sense that the soft/hard bands are less correlated at negative lags, but more correlated at positive lags  $\geq 1$  h.

This behavior, a peak at lag zero and a skewed CCF, has been observed many times. Ravasio et al. (2004) showed that such a shape can be reproduced by assuming flares that have the same form, a linear rise and exponential decay, but with different amplitudes and rise/decay time scales in the two energy bands. This explanation certainly works in the case of well sampled isolated flares. Here, we do not focus on single events but rather use the whole light curve to estimate the CCFs. The observed light curves are characterized by many “events” rising or decaying on different time scales, suggesting that more than one emission region is in operation in the system. The emission mechanism in one of them may operate on time scales equal to/longer than the duration of the light curves. It causes the larger amplitude variations which happen in phase in both energy bands, hence the zero lags when we integrate over the whole length of the observation. On the other hand, emission from other regions may operate on shorter time scales, causing changes of the emission pattern during the observation on a “characteristic time” scale of just a few ks. The physical meaning of this characteristic time scale is not obvious. Observationally, in the present data it could correspond to the duration of the flare-like events of relatively regular shape in the light curves which is equal to a few thousand ks. It is possible that this time scale corresponds to the size of the individual emission regions in the source. Weaker, shorter (i.e.

on time scales of seconds) variability might remain undetected in the measurement noise. On the other hand, there are also longer time scales in the system as, for example, the large scale variations during orbit 807 demonstrate. We now investigate whether the correlation properties of the emission in the two energy bands do evolve on periods comparable to this “few thousand second” time scale.

Long integration intervals were required in the past to obtain an acceptable signal to noise ratio with the limited photon statistics of previous instruments. The largely increased sensitivity of XMM–Newton allows the analysis of much shorter data streams. Brinkmann et al. (2003) split the individual Mrk 421 observations into two or three sub-intervals with similar variability patterns and flux levels and found differing CCFs for these sub-intervals.

Here we will employ a “sliding window” technique and calculate the CCFs for shorter data intervals, which start at different times of the observed light curve and range over a restricted time interval. Thus, the above defined  $CCF(k)$  will then be replaced by a  $CCF(k; \mathcal{T}, \mathcal{L})$ , i.e., the cross-correlation coefficient at a lag “k” is calculated for a data stream with length  $\mathcal{L}$  which starts at the time  $\mathcal{T}$  in the light curve.

In Fig. 4 we show a two dimensional representation of these sliding window CCFs, based on light curves with 10 s binnings. The vertical scale represents the lags (similar to the x-axis of Fig. 3), the color coding indicates the amplitude of the cross-correlation coefficient, with the color code given in the lowest panel of the figure. Time is along the x-axis. In the top figure the length of the individual data sets is  $\mathcal{L} = 2000$  s (thus the longest part of the light curve is covered), for the middle it is 6000 s and for the bottom figure 20 000 s. Clearly, in the first figure,  $CCF(k; \mathcal{T}, 2000)$ , the cross-correlation coefficient is very noisy, the CCF is dominated by local fluctuations and the data length  $\mathcal{L}$  seems to be shorter than the typical variability time scale. The middle panel ( $\mathcal{L} = 6000$  s) shows varying lags of both signs with different amplitudes as well as periods where there is hardly any inter-band correlation. This length seems to be in the range of the variability time scale of the source and it further demonstrates that the physical conditions of the emission regions change on that time scale. In the bottom figure the integration length of  $\mathcal{L} = 20\,000$  s over the data stream is obviously much longer than the variability time scale. Local variations of the sign and amplitude of the lags are smoothed out and produce cross-correlations with lags around zero, with an asymmetric amplitude distribution as found in Fig. 3.

The above discussion shows that there is an optimal window length  $\mathcal{L}$  which reveals best the time evolution of the CCF structure. In order to determine this length we regard the values (“response”) of the “local” cross correlation functions,  $CCF(k)$ , in all sliding windows for lags  $-2000\text{ s} \leq k \leq +2000\text{ s}$  as a probability distribution function (PDF),  $P(\text{ccf})$ , of different response values ranging from  $-1$  to  $1$ . By determining the statistical properties of these PDFs as a function of  $\mathcal{L}$  we can identify the optimized size of  $\mathcal{L}$ . If the sliding window is very small, only small correlations between the bands can be identified, because the CCF is dominated by the random fluctuations of the experimental noise. This results in a relatively narrow PDF peaking at  $P(\text{ccf}) \approx 0$ . If  $\mathcal{L}$  is very large, one is no longer

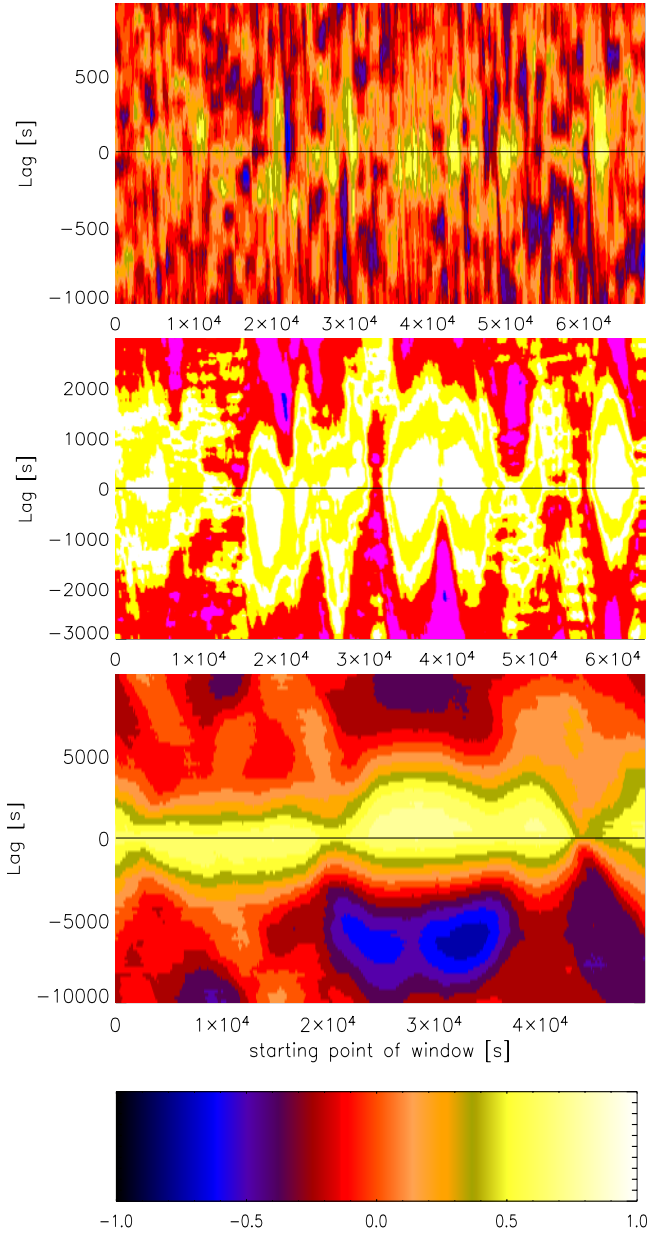


**Fig. 4.** Sliding window CCFs for orbit 546. The amplitude of the CCF is color coded, with lags plotted in the vertical direction. The top figure was calculated with an individual data length of 2000 s, the middle with 6000 s, and the bottom figure with 20 000 s long data streams. The bottom panel shows the color bar used for the numerical values of the CCFs for the above figure and for Fig. 6.

sensitive to the temporal fluctuation of the CCF, which may vary with appearing or disappearing flare events. Only an overall “mean cross correlation” between the bands is measured. The resulting PDF is also narrow but with a maximum at high values accounting for the obvious fact that there is an overall correlation between the energy bands. However, if the sliding window has an intermediate “optimal” length one is sensitive to the variations of the CCF, if present. The resulting  $P(\text{ccf})$  becomes broad with CCF-values covering a large part of the whole possible range and no pronounced maximum. To quantify this anticipated behavior of the PDFs we calculated their

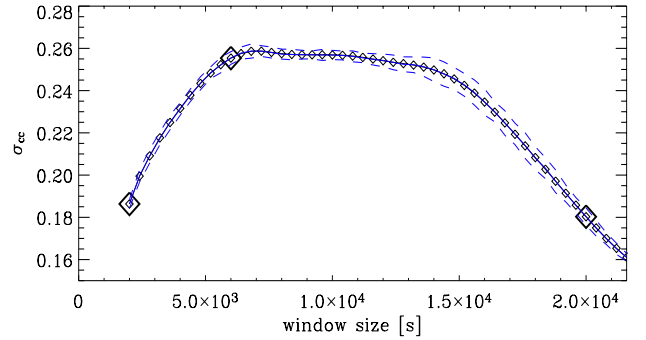


**Fig. 5.** Standard deviations  $\sigma_{P(\text{ccf})}$  of the sliding window CCFs for orbit 546 for different data lengths  $\mathcal{L}$ . The diamonds are the measured values, the three large symbols indicate the window lengths used for the CCFs in Fig. 4. The solid line gives the mean and the dashed lines the standard deviation of the re-sampled CCFs (see text).

standard deviation  $\sigma_{P(\text{ccf})}$  and plot them as a function of the sliding window sizes,  $\mathcal{L}$  (Fig. 5). The shape of the curve shows a broad maximum with the highest value at a window length  $\mathcal{L} \sim 7.2$  ks. At window sizes greater than  $\sim 15$  ks the standard deviations gradually decrease.

To verify that the observed behavior is of physical nature and not caused by statistical effects, namely less sampling for larger window sizes, we performed the following validation, which is inspired by ideas from bootstrapping (Efron 1993): for each window size we randomly selected as many CCFs as we have for the largest window size, and use them as the basis for the calculation of the standard deviation. This procedure enables us to determine a kind of bootstrap-error of the calculated  $\sigma_{P(\text{ccf})}$  by repeating the re-sampling procedure many times and calculating statistical means and standard deviations of the measured quantity sigma. The results are shown in Fig. 5 as the three lines (mean and standard deviations). It is obvious that we obtain the same results as previously, when the number of windows changed with  $\mathcal{L}$ .

Therefore, the highest variations in the  $\text{CCF}(k; \mathcal{T}, \mathcal{L})$  at a window length  $\mathcal{L} \sim 7.2$  ks truly indicate that this value matches the typical time scale in the light curve and that cross correlation functions calculated over the total light curve (i.e.  $\gg 20$  ks) provide only little information.

For the two other orbits a similar behavior was found with slightly different values for the maximal values (orbit 84: peak at 5.2 ks; orbit 807: peak at 10 ks). In Fig. 6 we show the CCFs for all three orbits calculated with these three optimized window sizes, for orbits 084 (top), orbit 546 (middle) and orbit 807. Again the amplitude of the CCF is color coded, with lags plotted in the vertical direction. Below the individual CCFs we show the corresponding light curves in the total (0.6–10 keV) energy band. The  $x$ -axis is the time from the beginning of the observation which, for the CCFs, corresponds to the start time of the CCF calculation. The light curves end at the time given by the difference of the observing time and the length of the sliding window.

The plot clearly demonstrates the complex behavior of the energy resolved light curves and the considerable uncertainties interpreting them. Let us note some peculiarities which are hard

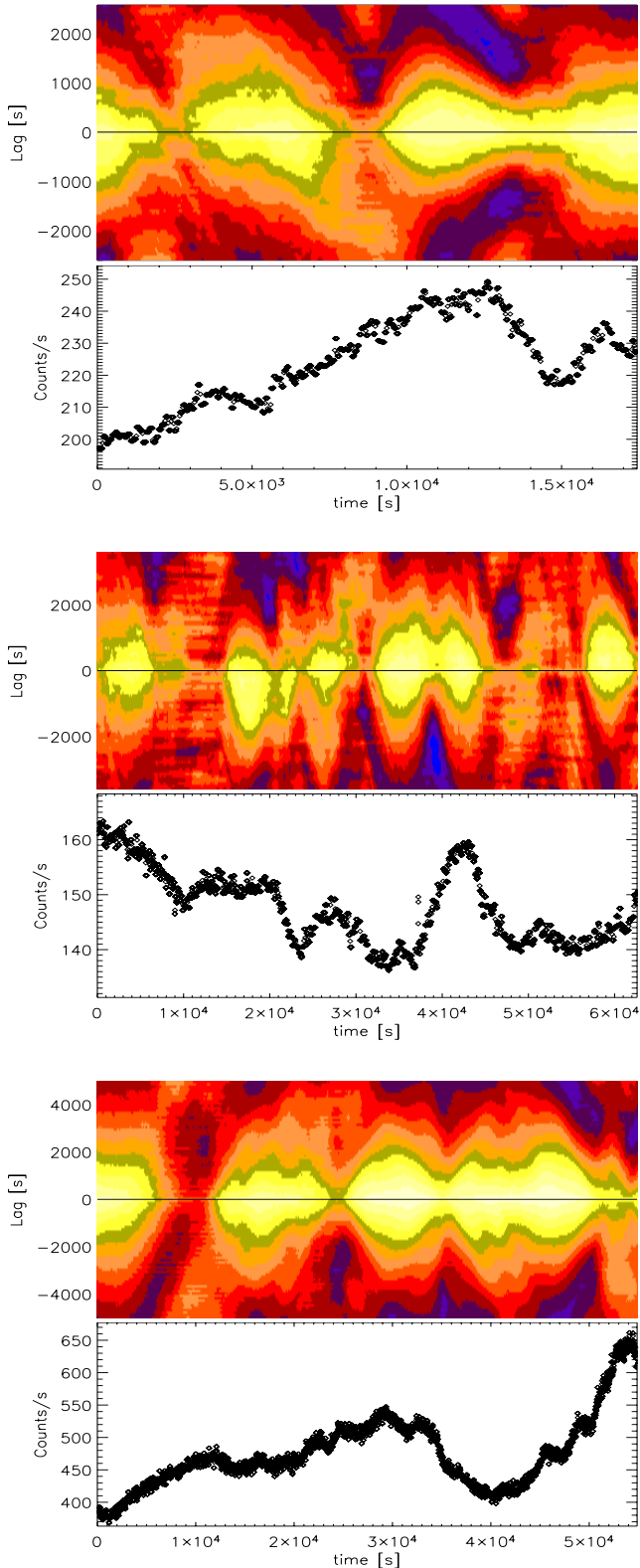


**Fig. 6.** Sliding window CCFs for orbits 084 (*top*), orbit 546 (*middle*) and orbit 807 (*bottom*) calculated with the optimized sliding window lengths (see text). The amplitude of the CCF is color coded, with lags plotted in the vertical direction. Plotted below the individual CCFs are the corresponding light curves in the total (0.6–10 keV) energy band. The  $x$ -axis is the time from the beginning of the observation which, for the CCFs, corresponds to the start time of the data window for the calculations.

to accommodate in “standard” scenarios of the emission from the BL Lac jets:

*Orbit 084:* Generally, there are always nearly zero lags between the two energy bands. The correlation coefficient tends to zero from times  $t \sim 2$ –3 ks, at the small bump in the light curve, and at around 8–9.5 ks, at the continuously increasing part of the light curve. As the data length  $\mathcal{L}$  of orbit 084 is taken to be 5.2 ks, the CCF at  $\sim 2$  ks, where it changes from highly correlated to weakly correlated, is calculated from data between 2–7.2 ks; that where it changes back between  $\sim 3$ –8.2 ks. Therefore, the data segments that can cause those changes are either between 2–3 ks or between 7.2–8.2 ks, i.e., at the beginning or at the end of the data sets. The light curve does not provide a clear answer to this question; however, the time resolved spectroscopy (see next section, Fig. 7) clearly points to a short hard flare centered at  $t \sim 3.5$  ks. The final parts of the CCF at times  $\geq 10^4$  s, which cover the intensity drop by about 25% at  $t \geq 13$  ks and the subsequent recovery of the count rate indicate that these flux variations have occurred at nearly zero lags.

*Orbit 546:* A small positive lag at the beginning, followed by zero lags during the following plateau phase. The intensity drop at  $t = 20$  ks results in a strong negative lag, while the increase and the subsequent decrease at  $t \geq 38$ –45 ks results in positive lags. The final parts of this decrease and the small substructure at  $\sim 51$  ks seem to have occurred nearly uncorrelated at the two energy bands. Note that the absolute variability amplitude during this observation is relatively small.

*Orbit 807:* The orbit where the source is brightest and exhibits the largest variability. Correlated at near-zero lags at the beginning and then, around the turning point of the flux increase, an extended period of very low correlation. The large variability region at  $t \geq 30$  ks seems to have occurred in both energy bands without strong time lags. However, the broadness of the correlation function at these later periods could indicate that the time scales of the smaller intensity fluctuations are not resolved.

These investigations lead us to the conclusion that, quite generally, an analysis of light curves in different energy bands might be inconclusive; in particular, when rapid and strong intensity variations cannot be resolved temporarily, for example, due to a low signal to noise ratio. The above CCF results demonstrate the complexity of the observed variations of the light curves in different energy bands but do not provide further information on the spectral behavior. An intensity decrease/increase is once accompanied by soft/hard lags (respectively) and once occurs nearly achronically. A more detailed understanding of the variability behavior of the source can be achieved with a study of the variations of the spectral slopes on time scales as short as possible, which we present below.

#### 4. Time-resolved spectroscopy

The observed count rates in the PN camera are high enough to study the energy spectrum of Mrk 421 over short periods of time in order to investigate in detail its spectral variability properties. To this end, we extracted energy spectra over the short observation intervals between the gaps that are introduced

when the detector falls into counting mode (see Sect. 2 above). The typical duration of these intervals are  $\sim 100$  s, 80 s and 20 s for the observations of orbit 84, 546 and 807, respectively. To avoid insufficient signal for extremely short EOIs we had to add in some cases subsequent data intervals to get the above-mentioned “typical” data stretches. Thus, for orbit 84 we fitted 149 individual data segments, 476 for orbit 546 and 456 for orbit 807. The number of photons for the individual fits in the 0.6–10 keV band were between 15 000 and 30 000, which is large enough to perform a meaningful model fitting to each spectrum individually. We used the same response matrices as for the total energy spectrum (see Sect. 2.2) and again fitted a broken power law model.

As a first test of the physical relevance of our results we investigated the best fit normalization values. We found an excellent correlation between these values and the observed count rate in the 0.6–10 keV energy band indicating that the observed flux variations are mainly caused by variations in the power law normalization (as opposed to spectral slope variations).

In most cases, the best fitting break energy value turned out to be in the range between 1.5–5 keV, i.e. similar to the values we found for the fits to the total energy spectra of the source. In some cases though, the full band energy spectrum could be quite well fitted by a single power law, and thus either the hard or soft spectral slopes ( $\Gamma_{\text{hard}}$  or  $\Gamma_{\text{soft}}$ , respectively) were determined with significant uncertainty. Furthermore, in most cases the best fitting  $\Gamma_{\text{hard}}$  and  $\Gamma_{\text{soft}}$  values are not different by more than  $\sim 1 - 2\sigma$ . This is due to the fact that the uncertainty associated with the hard band spectral slope is often quite large which is a direct result of the fact that most of the photons in the individual spectra are in the soft energy band. However, as our aim is to investigate the intrinsic temporal variations of the spectral “shape” of the source, the somewhat larger uncertainties of the individual best fitting slope values are not so important. What is important is to investigate whether the best fitting values are *systematically* different between successive data stretches, and if so, in what way.

Due to their large uncertainties and the existence of a few outliers, the light curves of the best fitting hard and soft slope values are noisy. For that reason we binned the respective light curves by calculating the weighted mean of 4 consecutive slope estimates in the case of orbits 84 and 807 observations and of 12 values for orbit 546. As a result, we are able to study the spectral slope variations of the source on time scales as short as  $\sim 500$  s and  $\sim 700$  s in the case of orbits 84 and 807, and  $\sim 180$  s for orbit 546. The bottom panels in Figs. 7–9 show plots of the binned  $\Gamma_{\text{hard,soft}}$  light curves. The soft and hard band count rate light curves are plotted in the top panels of the same figures.

These figures show clearly that apart from the strong, fast flux variations, Mrk 421 also exhibits significant spectral variations on time scales as short as  $\sim 500$ – $1000$  s. To the best of our knowledge, this is the first time that these quantitative spectral variations on time scales of a few hundred seconds have been studied along with the flux variations. We observe significant slope variations with a max-to-min variability amplitude of the order of  $\sim 7$ – $10\%$  and  $\sim 4$ – $6\%$  in the hard and soft slope light curves, respectively, for orbits 84 and 546. Apart from the largest amplitude flux variations, orbit 807, when the source is

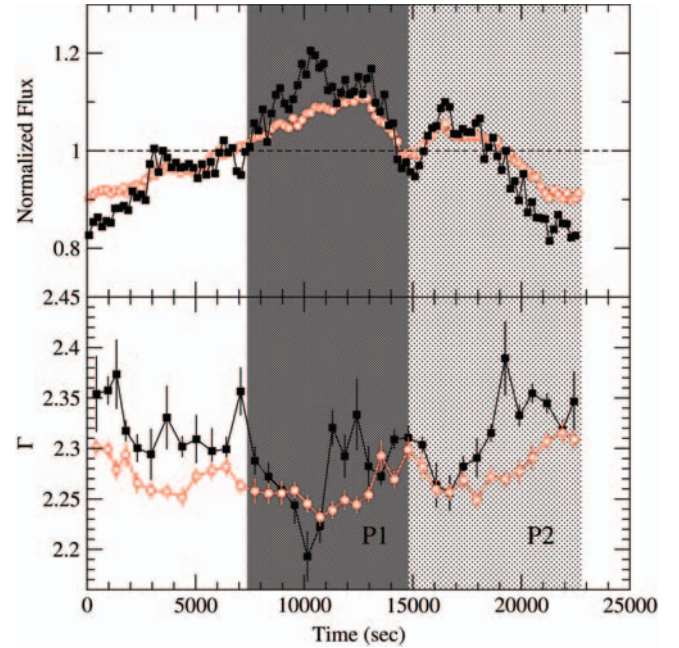


**Fig. 7.** Background subtracted, 0.6–2 and 4–10 keV PN light curves of Mrk 421 in orbit 84 (open circles and filled squares, respectively), in bins of size 200 s (*top panel*). The light curves are normalized to their mean. The corresponding  $\Gamma_{\text{hard}}$  and  $\Gamma_{\text{soft}}$  curves (filled squares and open circles, respectively) are plotted in the bottom panel (binned as described in the text). The shaded boxes identify those parts of the observation where the  $\Gamma$  vs. source flux relation is studied in more detail (see Sect. 4.1).

at its brightest state, shows the largest amplitude spectral variations as well: the max-to-min amplitude is  $\sim 30\%$  and  $\sim 20\%$  for the  $\Gamma_{\text{hard}}$  and  $\Gamma_{\text{soft}}$  light curves, respectively. In all cases, the hard band slope variations are of larger amplitude when compared with the soft band slope variations. Furthermore, both of them are of smaller amplitude than the amplitude of the flux variations in the respective bands.

Apart from the significant, fast spectral variations, the bottom panels of Figs. 7–9 show that, most of the time, the hard and soft band slopes are *not* the same. This result justifies a posteriori the use of the broken power law model fit to the individual, time resolved spectra of the source. Although the uncertainties of the slope values from the fits to *each* individual spectrum are not negligible the availability of many spectra, *and* the use of a broken power law model, reveals clearly that the soft and hard band slopes differ in a *systematic* way. In most cases, the slope of the photon spectrum at hard energies is steeper than the soft band slope. There are cases though when the photon spectrum is well described by a single slope power law (for example the period between 20–30 ks after the start of the observation in orbit 807) and even cases when the hard band slope is *flatter* than the soft band slope (for example the period after the first 30 ks in orbit 807).

The light curves of the fitted break energies show significant variations which are neither correlated with the best fitting slopes nor with the sources’ flux states. This may well be representative of the intrinsic behavior of the source. On the other hand, as discussed in Sect. 2.2, the X-ray spectrum of

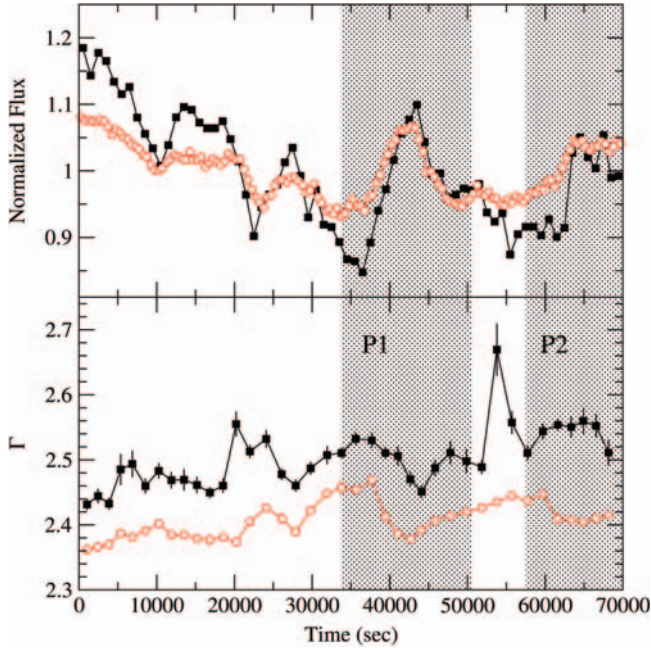


**Fig. 8.** Same as Fig. 7, but for the observation during orbit 546. The hard band and soft band count rate light curves are in bins of size 1000 s and 500 s, respectively.

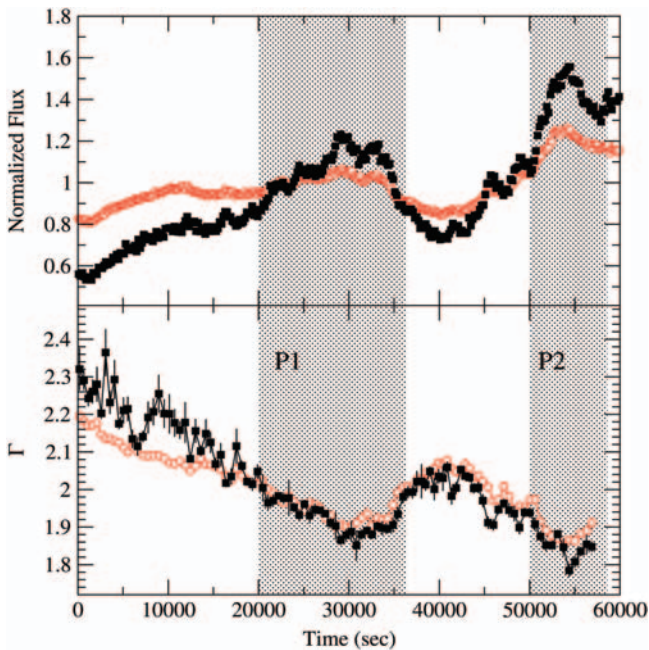


**Fig. 9.** Same as Fig. 7, but for the observation during orbit 807. The count rate light curves are in bins of size 40 s.

Mrk 421 may show a “continuous” curvature which the broken power law model can only approximate to some level. Thus, the break energy may not correspond to an intrinsic characteristic of the source, but may simply “divide” the spectrum into the two regions that show the largest difference in “curvature”. For this reason, we do not study the break energy variations hereafter. Instead, we concentrate on the study of the  $\Gamma_{\text{hard}}$  and  $\Gamma_{\text{soft}}$  variations, having in mind that these slopes simply give

a measure of the spectral curvature towards the soft and hard end of the X-ray spectrum.

#### 4.1. The relation between spectral and flux variations

“Hardness (or softness) ratio vs count rate” plots have been used in the past mainly to study the correlation between the flux and spectral variations in this source and other BL Lacs (see for example Brinkmann et al. (2003) and Ravasio et al. (2004) for a recent use of these plots with *XMM–Newton* data). In some cases, the evolution of the spectral slope itself as a function of the source flux has also been investigated. For example, Takahashi et al. (1996) studied the spectral slope variations of the source based on a day-long ASCA observation, Fossati et al. (2000b) used the best continuously curved model fits to study the spectral evolution on time scales of  $\sim 10$  ks, based on BeppoSAX observations, while Ravasio et al. (2004) have used simple power law fits to study the spectral variations during a few particular periods, chosen from two *XMM–Newton* light curves.

We believe that the analysis presented in the previous section provides a further improvement in these studies. Due to the high sensitivity of *XMM–Newton* we can probe spectral variations on time scales as short as  $\sim 1$  ks, based on model fitting results rather than on hardness ratios. By fitting a broken power law we are able to investigate separately the relation between the slopes of the soft and hard bands of the spectrum with the count rates in the respective energy bands. Also, we will study the cross-correlation between the soft and hard band slope light curves.

Figures 7–9 show that the hard and the soft band slope variations are correlated to a large degree. In general, both parts of the spectrum steepen or flatten at the same time, although not always at the same rate. There are cases when the hard and soft band variations are somehow “disconnected”. For example, in the period around 7 ks, between 11–13 ks and at 18 ks during orbit 84, we observe fast, large amplitude  $\Gamma_{\text{hard}}$  variations, which are absent in the  $\Gamma_{\text{soft}}$  time series. Similar events are observed in orbit 546, and at 7–11 ks in orbit 807. Not surprising, during the same periods, the peak in the CCF between the soft and hard band light curves is decreased (Sect. 3).

In order to investigate this anti-correlation further, we plot in Fig. 10 the slopes  $\Gamma_{\text{hard}}$  and  $\Gamma_{\text{soft}}$  as a function of the soft and hard band count rates, using all the data shown in Figs. 7–9. The top and middle panel in this figure show clearly the strong anti-correlation between the spectral and flux variations: both the hard and soft band spectra become harder as the flux decreases. This is a well known behavior for this source and other BL Lacs (cf. Pian 2002, and references therein; Brinkmann et al. 2003).

The flux-spectral slope relation is obviously not linear. Both the hard and the soft band slopes appear to “saturate” to the same limiting value of  $\Gamma \sim 1.8$  at the highest flux levels. This has already been observed in the past, see e.g. Ravasio et al. (2004). However, the large number of data points in Fig. 10 suggest a more complicated picture. For example, although most points in the spectral slope vs. flux plots do follow a power

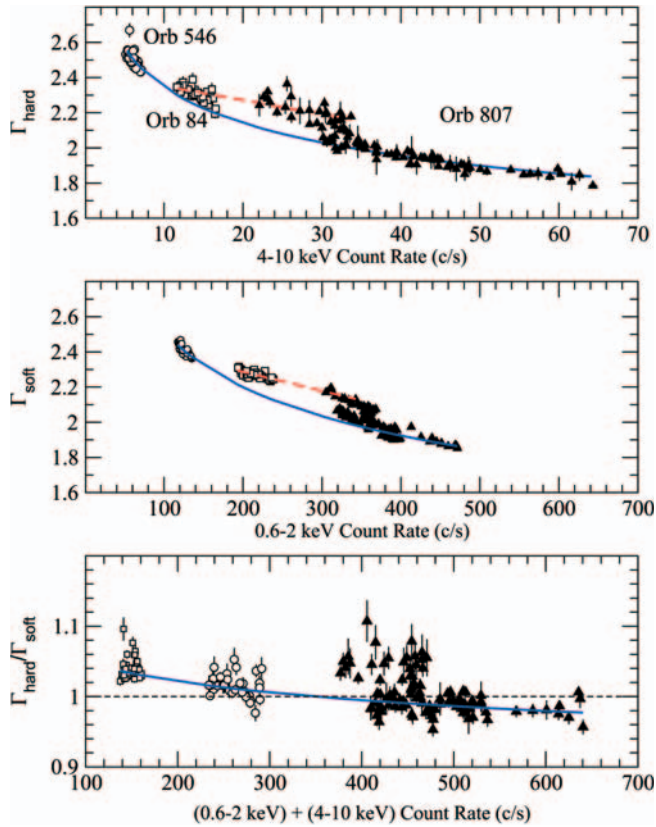


**Fig. 10.** The  $\Gamma_{\text{hard}}$  vs. 4–10 keV count rate and the  $\Gamma_{\text{soft}}$  vs. 0.6–2 keV relations (*top and middle panels*, respectively). The bottom panel shows the ratio  $\Gamma_{\text{hard}}/\Gamma_{\text{soft}}$  plotted as a function of the 0.6–10 keV count rate. Data points from Figs. 7–9 are shown with open circles, open squares and filled triangles, respectively. The solid curves describe broad trends as discussed in the text. For the orbit 84 observation, which was performed with a thick filter, the 0.6–2, 4–10 and 0.6–10 keV count rates are multiplied by factors of 1.22, 1.01, and 1.19, respectively. These are the count rate ratios expected for the thick and medium thick filters in the case of a power law spectrum and  $N_{\text{H}}$  similar to that of Mrk 421.

law like relation (shown with the solid lines in the two upper plots), in other cases a linear relation appears to describe the data better. It seems possible that there are various well defined paths (i.e. “spectral states”) in the “ $\Gamma$  vs. flux” plane that the source follows at different times.

The bottom panel in Fig. 10 shows a plot of the ratio  $\Gamma_{\text{hard}}/\Gamma_{\text{soft}}$  versus the total (i.e. 0.6–10 keV) source count rate. We find that the slope ratio does not remain constant, but rather decreases with increasing source flux. A power law model (shown as a solid line in this panel) appears to be broadly consistent with the decrease of the slope ratio as the source flux increases, although not all points follow the same trend.

#### 4.2. Temporal correlations of the spectral variations

To investigate whether the spectral and flux variations happen simultaneously, we computed the cross-correlation function (CCF) between the spectral slope and count rate light curves shown in Figs. 7–9. We used the “Discrete Correlation Method” of Edelson & Krolik (1988), with a lag size of

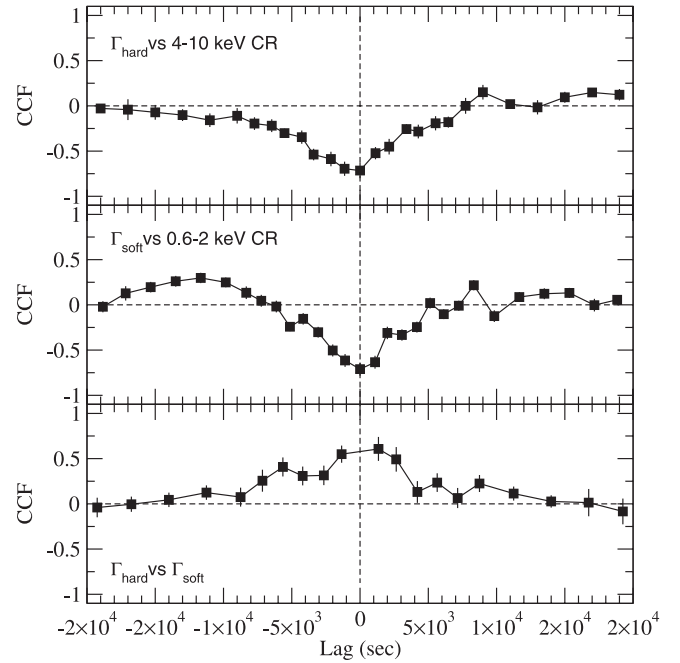


**Fig. 11.** The average cross-correlation function between  $\Gamma_{\text{hard}}$  and 4–10 keV count rate (*top panel*), the  $\Gamma_{\text{soft}}$  and 0.6–2 keV count rate (*middle panel*), and between the two spectral slopes  $\Gamma_{\text{hard}}$  and  $\Gamma_{\text{soft}}$  (*bottom panel*), using data from all observations. The CCFs are defined such that any positive delays would imply a delay of the spectral with respect to the flux variations (in the upper two panels), and a delay of the  $\Gamma_{\text{hard}}$  with respect to the  $\Gamma_{\text{soft}}$  variations, in the bottom panel.

$\Delta k = 800$  s, 1000 s, and 500 s in the cases of orbits 84, 546 and 807, respectively. We also computed the DCF between the  $\Gamma_{\text{hard}}$  and  $\Gamma_{\text{soft}}$  light curves, to examine the simultaneity of the different band slope variations. Note that in this case we did not estimate the CCF at lag zero, because the slopes were obtained from model fitting to the same spectrum and any correlated, systematic biases in the estimation of  $\Gamma_{\text{soft}}$  and  $\Gamma_{\text{hard}}$  can artificially increase the CCF value at this lag.

The cross correlation functions of all three observations look very similar. For that reason, in order to increase the signal-to-noise, we combined the three individual  $\Gamma_{\text{hard}}/\Gamma_{\text{soft}}$  vs. flux and the  $\Gamma_{\text{hard}}$  vs.  $\Gamma_{\text{soft}}$  CCFs into one file, respectively, and estimated average CCFs in each case. The average  $\Gamma_{\text{hard}}$  vs. flux,  $\Gamma_{\text{soft}}$  vs. flux and  $\Gamma_{\text{hard}}$  vs.  $\Gamma_{\text{soft}}$  CCFs are shown in Fig. 11. The highest peak is at lag  $\sim 0$  in all cases, suggesting that any delays between the slope and flux variations, or between the soft and hard band slope variations, should be shorter than  $\sim 1000$  s. The CCFs look fairly symmetric around zero lag suggest that both the hard and soft band spectra and flux variations happen almost simultaneously, to the limit of the current temporal resolution.

#### 4.3. The shortest time scales

Although the results from Sect. 4.1 show that, in general, the spectrum hardens as the source flux increases, the  $\Gamma$  vs. flux behavior of the source is quite complicated during individual “events”. For that reason, we now focus our study of the

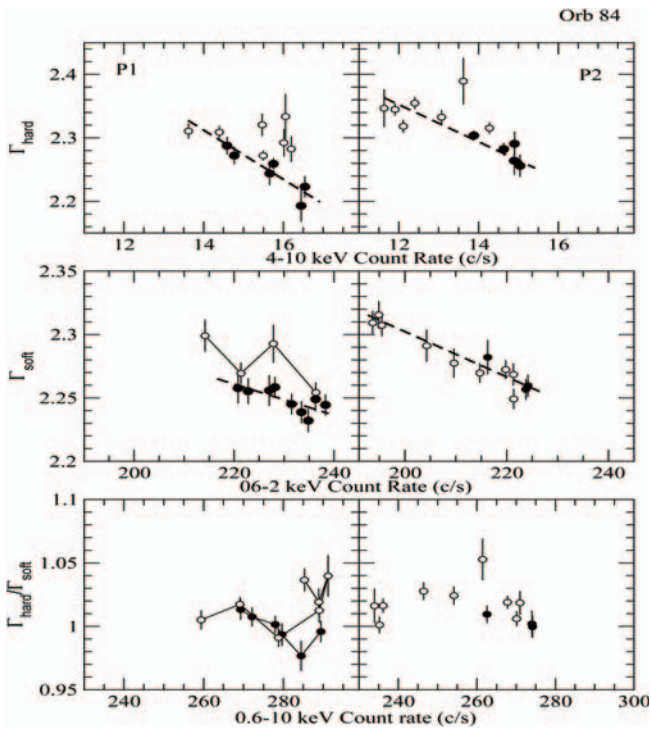


**Fig. 12.** Orbit 84: the  $\Gamma_{\text{hard}}$  vs. 4–10 keV count rate and the  $\Gamma_{\text{soft}}$  vs. 0.6–2 keV relations (top and middle panels, respectively) for the “P1” and “P2” parts (identified by the shaded boxes in Fig. 7). The bottom panel shows the ratio  $\Gamma_{\text{hard}}/\Gamma_{\text{soft}}$  as a function of the 0.6–10 keV count rates. Filled circles show the data points during the flux rise and open circles during the decaying phase of each event. The dashed line indicates the linear path that the rising (or the decaying) phase points follow. For clarity, in cases where the two phase points follow different paths, or define loop-like structures, the respective points are connected with solid lines.

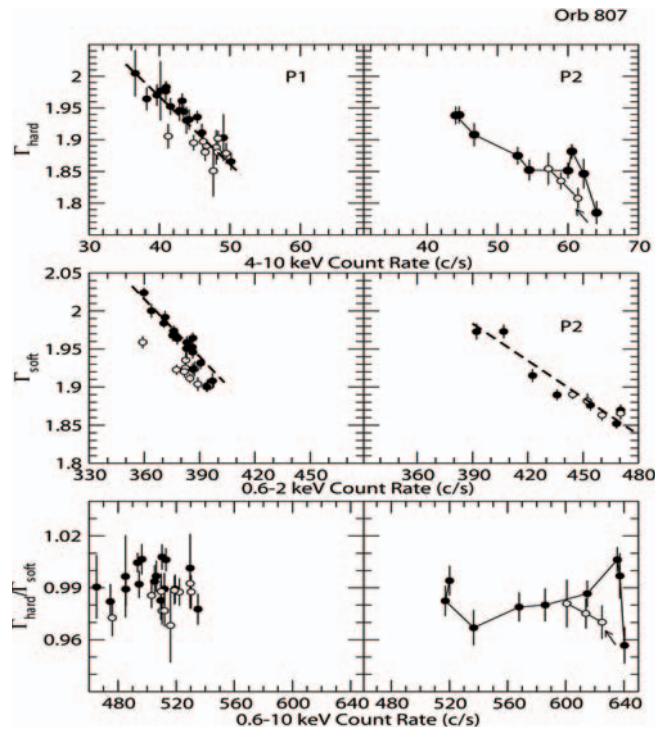


**Fig. 14.** Same as Fig. 12, but for the parts “P1” and “P2” in orbit 807.

spectral variability behavior of the source during the periods which are marked with shaded boxes in Figs. 7–9. These correspond to well defined, single “flare-like” events, where both the flux rising and decaying parts have been adequately sampled (with the exception of the P2 event in orbit 546, where it is not clear whether the flux has started decreasing or not). Figures 12–14 show the  $\Gamma_{\text{hard}}$  vs. 4–10 keV count rate (top), the  $\Gamma_{\text{soft}}$  vs. 0.6–4 keV (middle) and the  $\Gamma_{\text{hard}}/\Gamma_{\text{soft}}$  vs. 0.6–10 keV (bottom panels) during these events. Filled and open circles correspond to data points during the flux rise and decay phases, respectively.

The results from the analysis presented in this section are complementary to those presented in the past (e.g. Takahashi et al. 1996; Fossati et al. 2000b; Ravasio et al. 2004). However, they also provide some new insight into the source’s behavior. By a) studying all flaring events that we could identify in the *XMM–Newton* light curves, by b) using spectral slope estimates in two energy bands on time scales as short as  $\sim 1$  ks, and by c) combining spectral with timing information (from Sect. 3) we demonstrate that the source does *not* operate in the same way at all times.

Our results in the case of the P1 flare during orbit 546 are in agreement with the results of Ravasio et al. (2004). Although our model fitting results show clearly that the the soft and hard band parts of the spectrum have different slopes, both  $\Gamma_{\text{hard}}$  and  $\Gamma_{\text{soft}}$  follow a clockwise loop pattern during the evolution of the flare. In fact, even the  $\Gamma_{\text{hard}}/\Gamma_{\text{soft}}$  ratio follows a clockwise loop as the flare evolves. As the flux rises, both the soft and hard band spectra flatten, but at different rates:  $\Gamma_{\text{soft}}$  flattens faster. When the flux decreases the spectra become steeper, but  $\Gamma_{\text{hard}}$  steepens faster than  $\Gamma_{\text{soft}}$ , and the slope ratio decreases for a while. Finally, it increases again as  $\Gamma_{\text{hard}}$  does not vary

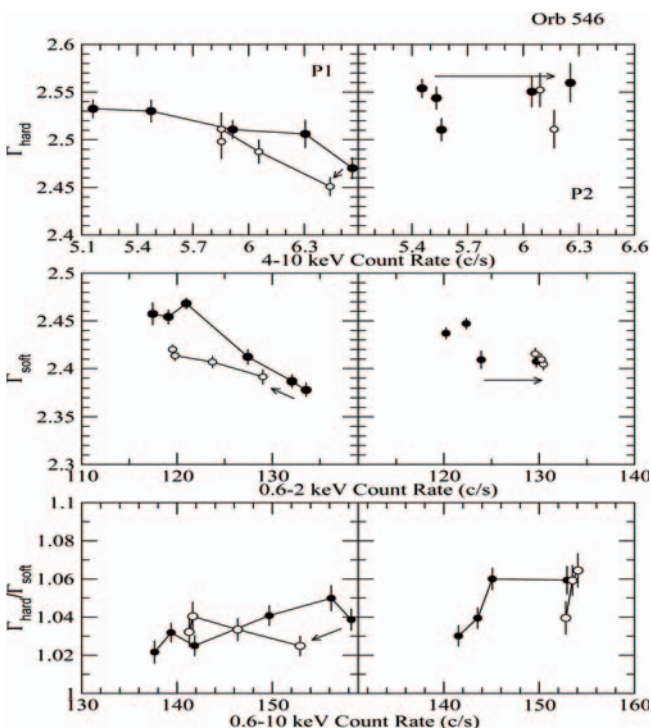


**Fig. 13.** Same as Fig. 12, but for the parts “P1” and “P2” in orbit 546.

appreciably any more while  $\Gamma_{\text{soft}}$  still increases. The CCF results suggest hard lags during the same period (see Sect. 3), a result that is consistent with the spectral evolution behavior of the source: variations are propagated from the softer to the harder energy bands during the initial flux rising phase, and then the hard band flux decays faster than the soft band flux.

However, the source does *not* show the same behavior at all times. For example, during the P1 flare in orbit 807 the  $\Gamma_{\text{hard}}$  variations follow the same path during the flux rise and decay phase (shown with the dashed line in the top left panel of Fig. 14). No loop patterns are observed in the  $\Gamma_{\text{hard}}/\Gamma_{\text{soft}}$  ratio either; the slope ratio remains roughly constant, implying that the hard and soft band spectra evolve at the same rate. The CCF results imply no delays between the variations observed in the two bands. A similar behavior is also observed during the P2 flare in orbit 84. Both  $\Gamma_{\text{hard}}$  and  $\Gamma_{\text{soft}}$  evolve in the same way during the rising and decaying phases (dashed lines in the top and middle right panels in Fig. 12). Consequently, the slope ratio remains roughly constant as the flare evolves. In agreement with the observed spectral variability behavior, the CCF analysis shows no delays between the hard and soft band during this event.

The P1 flare in orbit 84 is a case where obvious variations in  $\Gamma_{\text{hard}}$  are not evident in the  $\Gamma_{\text{soft}}$  time series. The dashed line in the top left panel in Fig. 12 shows the  $\Gamma_{\text{hard}}$  variations as the flux increases (filled circles). Some of the  $\Gamma_{\text{hard}}$  values during the flux decay phase do follow the same path, but most of the  $\Gamma_{\text{hard}}$  values during the prolonged “flare-plateau” phase between 11–13 ks (Fig. 7) are clearly not consistent with it. Furthermore, the  $\Gamma_{\text{soft}}$  values during flux decay lie systematically above the  $\Gamma_{\text{soft}}$  values in the rising phase suggesting the presence of an anti-clockwise loop pattern. As a result of these two effects, the slope ratio also follows a loop pattern, which evolves in an anti-clockwise direction. The P2 flare in orbit 807 is another case of a flare where the  $\Gamma_{\text{hard}}$  and  $\Gamma_{\text{soft}}$  variations do not show the same behavior: the former follows a clockwise loop pattern (top right panel in Fig. 14), while the  $\Gamma_{\text{soft}}$  evolution follows the same linear path in both the rising and decaying flare phases.

That obvious case where the hard and soft band slopes are almost entirely “disconnected” is the P2 event in orbit 546. Initially,  $\Gamma_{\text{hard}}$  steepens ( $\Delta\Gamma \sim -0.05$ ) and  $\Gamma_{\text{soft}}$  flattens ( $\Delta\Gamma \sim 0.05$ ) although the flux does not change appreciably. Then, both slopes remain constant during a  $\sim 15\%$  and  $\sim 8\%$ , rapid hard and soft flux increase, respectively. Towards the end of the observation,  $\Gamma_{\text{soft}}$  remains constant, while  $\Gamma_{\text{hard}}$  flattens slightly (right panels in Fig. 13). However, the slope ratio changes imply that these apparently different variations are in fact “connected” in some way. A well defined loop pattern appears in the slope ratio evolution plot which implies that the variations are propagated from the soft to the hard band. This result is also supported by the strong, hard lags that are observed in the same period (see Sect. 3).

## 5. Discussion

In this work we presented a spectral and timing analysis of the three calibration phase XMM–Newton observations of

Mrk 421 performed in timing mode. The analysis strongly relied on that mode as, for example, the enormously high count rates of  $\sim 800$  cts/s in orbit 807 would have led to a substantial photon pile up – even in the extremely short frame time of  $\sim 5.7$  ms of the PN small window mode and thus to a large reduction of photons available for the analysis.

Our average results confirm and, in a way, expand the findings of previous XMM–Newton investigations of Mrk 421 (Brinkmann et al. 2001; Sembay et al. 2002; Brinkmann et al. 2003; Ravasio et al. 2004) and earlier extended studies with ASCA and BeppoSAX. In the following we summarize our main findings which might help to understand the complex behavior of the source.

### 5.1. The CCF results

In general, the observed soft and hard band variations are well correlated in all three observations. However, using a sliding window cross-correlation analysis, we could show that the cross links between the soft and the hard bands are really complicated and not easily understood. There exists a “characteristic” time scale (of the order of a few ksec) on which the CCF appears to change “continuously” and, depending on the length of the observing window and the actual activity state of the source, we find periods with positive or negative or no lags, but also periods of weak correlations between the soft and hard energy bands:

- Periods of weak correlations appear when variations in the hard band flux or hard band spectra slope are absent in the soft band.
- Strong correlation with no obvious lags is observed throughout orbit 807, although the flux does go up and down. In fact, this orbit shows the highest amplitude flux variations!
- In cases where we observe the soft leading the hard band variations (e.g. P1 and P2 in orbit 546) or the hard leading the soft (e.g. at  $\sim 23$  ks in orbit 546) the delays are just a few minutes in agreement with the lags already noticed by Brinkmann et al. (2003).
- The analysis of orbit 84 shows a much more complicated picture than anticipated from Brinkmann et al. (2003) where the observation was split in only two parts. Here we find the hard flux leading the soft at the beginning, then loss of correlation, then the soft flux leading, then the hard leading briefly, and then a loss of correlation in the prolonged “flare plateau” phase, where the hard band variations are absent in the soft band.

There is, certainly, a continuous range of variability time scales, as seen for example in orbit 807, and up to a day or longer (Kataoka et al. 2001). However, the abovementioned “characteristic” time scale of correlated emission, i.e., the time scale over which the correlation between hard and soft band emission is found to exist, to change sign, or to disappear, might be representative for the size of the individual emission regions. With a bulk Lorentz factor of the jet of  $\Gamma \sim 10$  this would correspond to an emission region of a few  $\times 10^{15}$  cm.

### 5.2. The relation between spectral and flux variations

The cross-correlation analysis demonstrates, on the other hand, the limitations of this method as only little information about the actual spectral variations can be extracted. We therefore used the high signal to noise ratio to perform proper spectral fits to the data down to time scales of  $\gtrsim 20$  s. Mrk 421 shows significant spectral variations on time scales as short as  $\sim 500$ – $1000$  s and most of the time, the hard and soft band slopes are *not* the same. Generally, the slope of the photon spectrum at hard energies is steeper than the soft band slope but there are cases when the hard band slope is *flatter* than the soft band slope

The spectral behavior follows the well-known “the brighter the harder” trend. Both, the hard and the soft band spectral indices show a non-linear correlation with the source flux, and there is an indication that the source may populate different spectral states at different times in the “ $\Gamma$  vs. flux” plane. In general, as the flux rises, both the soft and hard band spectra flatten, but  $\Gamma_{\text{soft}}$  flattens faster. Then the spectra become steeper as the flux decreases, but now  $\Gamma_{\text{hard}}$  steepens faster than  $\Gamma_{\text{soft}}$ . On long time scales  $\Gamma_{\text{soft}}$  and  $\Gamma_{\text{hard}}$  vary in phase and they vary in phase with flux.

On shorter time scales, during the evolution of some flare like events, we observe “hysteresis” phenomena.  $\Gamma_{\text{soft}}$ ,  $\Gamma_{\text{hard}}$  and their ratios follow loop-like paths in the spectral vs. flux plots in the clockwise (P1 in orbit 546) and anti-clockwise (P1 in orbit 84) direction. In other cases though, both evolve on a straight line during rise and decay of the flux (P2 in orbit 84), we observe a flare where only one follows a loop (P2 in 807), and there is another case where only the slope ratios follow a well defined structure (P2 in orbit 546).

### 5.3. Implications to physical models

The numerous instances where the source does not follow the “average” standard pattern show that any determination of the physical parameters of the emission region from simple “homogeneous”, “one-zone”, etc., models might be questionable. There are cases, for example P1 and P2 in orb 546, which could be “flares” that correspond to emission from a single, perturbed region of the jet. They show hard lags, so the whole events are governed by the “acceleration” time scale of the relativistic electrons. Even the soft lags that we see during the flux drop before P1, could indicate evolution governed by the cooling time scale. Interestingly, these “clear” events show up when the source is at its lowest flux state. It could be that in these cases we have mainly only one region emitting at any time. In general, the complex spectral behavior indicates that the emission geometry is not that simple. At a time  $t_{\text{obs}}$  we are not only seeing the emission from a certain position  $R(t)$  in the relativistically moving jet, but as well the earlier emission from all positions  $\sim R - c \delta t$  down the jet. In the framework of the commonly accepted shock-in-jet model this emission is determined by the history of the colliding shells (blobs) – and, perhaps, by the earlier (or later) emission of other, independent shells.

Even in the framework of the basic, two-colliding-shells model (Spada et al. 2001), non-linearities are expected. Most of the emission is, certainly, generated when the second, faster

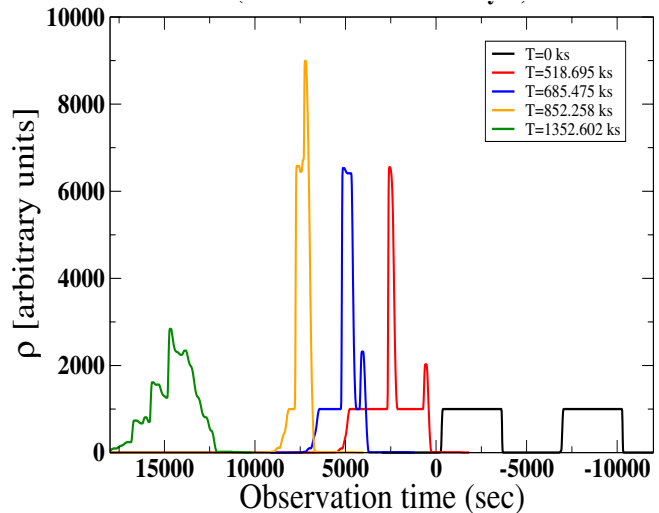


**Fig. 15.** Density (in arbitrary units) of the colliding shells at different evolution times (in the jet frame) of the system as seen by a distant observer. The observation time (with arbitrary origin) runs from right to left. The plot shows at what times the observer would “see” the various structures approaching him with relativistic velocities.

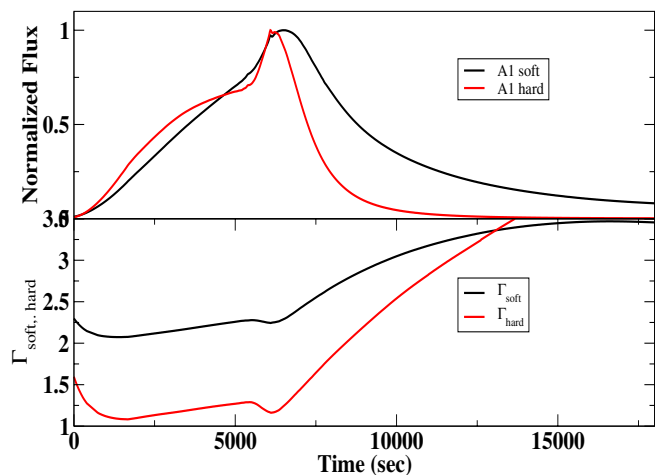


**Fig. 16.** Normalized X-ray emission from the model of Fig. 15 in the top panel in the hard (1–10 keV, red curve) and the soft (0.1–1 keV) X-ray band. The bottom panel shows the evolution of the spectral power law indices in the two bands.

shell hits the first, slower shell. Particles are accelerated, magnetic fields are amplified and part of the available energy of this shocked region is radiated. However, the first shell travels as well with supersonic speeds along the jet, a shock structure has developed at its front and a reverse shock travels back through the shell and, after some time, runs into the shocked emission region of the two colliding shells. Depending on the initial (and boundary) conditions of the system this might lead to noticeable changes of the physical state of the emission region and to “unexpected” changes of the emission characteristics.

These effects are illustrated in the following figures, obtained from numerical relativistic hydrodynamic simulations of two colliding shells with Lorentz factors  $\Gamma_1 = 5$  and  $\Gamma_2 = 7.5$  (Mimica et al. 2004a,b). Figure 15 shows the density distribution of the shells at five different times in the jet frame as seen

by a distant observer. The origin of the observer’s time scale is arbitrarily chosen. The configuration at  $T = 0$  in the jet frame (black curves) would be seen by a distant observer between  $-10\,000 \leq t_{\text{obs}} \leq 0$  s as two individual shells moving towards him. The situation at  $T \sim 519$  ksec in the jet frame (red curve) would first appear to the observer as the shock structure at the front of shell 1 and then, around  $t_{\text{obs}} \sim 2500$  s, as strongly rising emission as the two shells have collided. From then on, up to about  $t_{\text{obs}} \sim 5000$  s, the emission would be rising due to the growing density and size of the collision region in the jet frame. At  $t_{\text{obs}} \sim 7500$  s, at the evolutionary time  $T \sim 852$  ks in the jet frame (yellow curve), the shock structure from shell 1 has merged with the interaction region of the shells, changing strongly the emission properties. Then, at later times, the structure fades away.

Figure 16 shows the normalized light curve of this event in the 0.1–1 keV and the 1–10 keV X-ray band in the upper panel and the evolution of the spectral indices in the lower panel. It must be emphasized that the parameters chosen for this simulation are not at all applicable for the physical conditions in Mrk 421. The spectra indicate that the shocks are too strong and/or the magnetic field amplification has been overestimated; they are just presented for illustrative purposes. In particular, the spectral hardening phase occurs only at the very beginning of the rising light curve, then the spectrum starts cooling. At the time where the reverse shock from the first shell joins the inter-shell emission region, we find spectral and intensity changes of the emission which would not fit into a “regular” evolution pattern of the observed flare and the cross correlation analysis of this light curve would predict lags of changing sign and amplitude. Looking at the above presented observations it appears that, for example, parts of the light curve of orbit 807 (Fig. 9) resemble this behavior: the flux and spectral index of the soft energy band varies smoothly while the flux and power law index in the hard band exhibits some “unexpected” deviations.

One of the most interesting questions raised by the observed emission is the cause of the long-term intensity changes. In the three observations analyzed here, the flux changed by a factor of more than three. Are these variations caused by geometrical changes of the viewing conditions, like in the lighthouse model by Camenzind & Krockenberger (1992)? Or are we seeing periods of enhanced activity, a dramatic increase of the number of interacting blobs or stronger interactions – for which the individual emission patterns are averaged and form an enhanced “background” emission. There is growing evidence that the blazar emission consists of a “quasi-stationary” component which changes only on long time scales and a flaring component which gives rise to the short time scale intensity and spectral variations. The influence of these different components on the determination of the physical parameters deduced from the observations has been discussed in more detail by Fossati et al. (2000a) and Fossati et al. (2000b). In extensive numerical simulations of the shock-in-jet scenario, varying the injection rate, the duration, speeds and other relevant physical parameters of the shells, we could not reproduce the observed variability pattern of the emission of Mrk 421. Only after adding a substantial “background” emission of  $\geq 60\%$  to the

numerically estimated flux we did find light curves that looked similar to the observed ones.

## 6. Conclusions

We have presented a time resolved analysis of the currently available XMM-Newton observations of Mrk 421 performed with the PN in timing mode. The high signal to noise ratio allowed us to perform cross-correlation analyses between the soft and hard energy bands with a sliding window technique which revealed that the characteristics of the correlated emission changes on time scales of a few ksec. With time-resolved spectral fits on time scales of a few hundred seconds we could study the spectral evolution of the source. We find significant spectral variations on time scales as short as  $\sim 500$ – $1000$  s and non-linear correlations between between slopes of the fitted broken power law model and the flux of the source.

The temporal and spectral behavior of the source is very complex and during flares various variability patterns in the soft and hard energy band were observed. Correspondingly, it appears hard to deduce uniquely the underlying physical parameters for the emission process from the observations. We compared the observations with relativistic hydrodynamic simulations of the currently favored “shock-in-jet” model for the BL Lac emission (see, for example, Spada et al. 2001) which takes into account that we are seeing the emission from multiple shocks which have either very different physical parameters or that we detect the emission from similar shocks at very different states of their evolution, heavily confused by relativistic beaming and time dilatation effects. As the actual emission characteristics of these numerical models depend on a large number of physical parameters and poorly known boundary conditions it is a tedious task to reproduce numerically the large variety of observed light curves. However, BL Lac jets are relatively simple physical systems, which might be solely governed by the equations of relativistic MHD and special relativity. Thus, further observational progress (in particular long continuous XMM-Newton observations with high spectral and temporal resolution) and extended numerical simulations might finally lead to a better understanding of the physical conditions in these systems.

*Acknowledgements.* This work is based on observations with XMM-Newton, an ESA science mission with instruments and contributions directly funded by ESA Member States and the USA (NASA).

## References

- Brinkmann, W., Sembay, S., Griffiths, R. G., et al. 2001, A&A, 365, L162
- Brinkmann, W., Papadakis I., den Herder J. W. A., & Haberl, F. 2003, A&A, 402, 929
- Cagnoni, I., Papadakis, I. E., & Fruscione, A. 2001, ApJ, 546, 886
- Camenzind, M., & Krockenberger, M. 1992, A&A, 255, 59
- Cui, W. 2004, ApJ, 605, 662
- Edelson, R., & Krolik, J. H. 1988, ApJ, 336, 749
- Edelson, R., Griffiths, G., Markowitz, A., et al. 2001, ApJ, 554, 274
- Efron, B. 1993, An Introduction to the Bootstrap (New York: Chapman and Hill)

- Ehle, M., Breittellner, M., Dahlem, M., et al. 2001, XMM-Newton Users' Handbook, [http://xmm.vilspa.esa.es/external/xmm\\_user\\_support/documentation/uhb/index.shtml](http://xmm.vilspa.esa.es/external/xmm_user_support/documentation/uhb/index.shtml)
- Fossati, G., Celotti, A., Chiaberge, M., et al. 2000a, *ApJ*, 541, 153
- Fossati, G., Celotti, A., Chiaberge, M., et al. 2000b, *ApJ*, 541, 166
- Inoue, S., & Takahara, F. 1996, *ApJ*, 463, 555
- Kataoka, J., Takahashi T., Makino F., et al. 2000, *ApJ*, 528, 243
- Kataoka J., Takahashi T., Wagner S. J., et al. 2001, *ApJ*, 560, 569
- Malizia, A., Capalbi, M., Fiore, F., et al. 2000, *MNRAS*, 312, 123
- Maraschi, L., Fossati, G., Tavecchio, F., et al. 1999, *ApJ*, 526, L81
- Mimica, P., Aloy, M. A., Müller, E., & Brinkmann, W., 2004a, *A&A*, 418, 947
- Mimica, P., Aloy, M. A., Müller, E., & Brinkmann, W., 2004b, *Ap&SS*, 293, 165
- Papadakis, I., & Lawrence, A. 1995, *MNRAS*, 272, 161
- Pian, E., 2002, *Pub. Ast. Soc. Austr.*, 19, 49
- Punch, M., Akerlof, C. W., Cawley, M. F., et al. 1992, *Nature*, 358, 477
- Ravasio, M., Tagliaferri, G., Ghisellini, G., & Tavecchio, F. 2004, *A&A*, 424, 841
- Sembay, S., Edelson, R., Markowitz, A., Griffiths, R. G., & Turner M. J. L. 2002, *ApJ*, 574, 634
- Spada, M., Ghisellini, G., Lazzatti, D., & Celotti, A. 2001, *MNRAS*, 325, 1559
- Takahashi, T., Tashiro, M., Madejski, G., et al. 1996, *ApJ*, 470, L89
- Takahashi, T., Kataoka, J., Madejski, G., et al. 2000, *ApJ*, 542, L105
- Tanihata, C. 2002, Ph.D. Thesis Tokyo Univ., ISAS Research Note, 739
- Tanihata, C., Urry, C. M., Takahashi, T., et al. 2001, *ApJ*, 563, 569
- Tavecchio F., Maraschi L., & Ghisellini G. 1998, *ApJ*, 509, 608
- Ulrich, M.-H., Maraschi, L., & Urry, C. M. 1997, *ARA&A*, 35, 445
- Urry, C. M., & Padovani, P. 1995, *PASP*, 107, 803
- Zhang, Y. H., Celotti, A., Treves, A., et al. 1999, *ApJ*, 527, 719
- Zhang, Y. H., Cagnoni, I., Treves, A., Celotti, A., & Maraschi, L. 2004, *ApJ*, 605, 98